Influence of surface roughness on the deformation of gold nanoparticles under compression

Hugo Iteney, Thomas W Cornelius, Olivier Thomas, Jonathan Amodeo

H. Iteney, T.W. Cornelius, O. Thomas, J. Amodeo, Influence of surface roughness on the deformation of gold nanoparticles under compression, Acta Mater. 281 (2024) 120317. https://doi.org/10.1016/j.actamat.2024.120317.

Influence of surface roughness on the deformation of gold nanoparticles under compression

Hugo Iteney[a], Thomas W. Cornelius[a], Olivier Thomas[a], Jonathan Amodeo[a]

[a] *Aix-Marseille Université, Université de Toulon, CNRS, IM2NP, Marseille, 13013, France*

Abstract

The influence of surface roughness on the mechanics of Au-faceted nanoparticles under compression is investigated using molecular dynamics simulations. Results show an increasing impact of the surface roughness on the mechanical response while decreasing the roughness parameters with critical strength variations up to 90% of the one computed in case of flat-surface nanoparticles. Surface ledges act as stress concentrators and nucleation sites for the emergence of dislocations in regular 1/2<110>{111} slip systems and less common 1/2<110>{001}. Moreover, rough surfaces evolve continuously during deformation as influenced by a dislocation surface shearing process that impacts the dislocation nucleation process. Finally, the yield stress of nanoparticles shows a strong dependence to the true contact surface with two distinct regimes that depends on whether dislocations nucleate from an isolated surface atomic islet or from an edge-connected one. A model for strength prediction in nanoparticles relying on the surface topography is proposed. This study offers new perspectives on the interpretation of critical stress data scattering often measured in mechanical experiments performed at the nanoscale.

Keywords: Roughness, Nanoparticles, Molecular dynamics, Nanomechanics, Dislocations

Email address: jonathan.amodeo@cnrs.fr (Jonathan Amodeo)

1. Introduction

In recent years, micro- and nano-objects (particles, wires, films and pillars) have been the subject of particular interest in the field of small-scale mechanics because of their outstanding strength and ductility [1, 2, 3, 4, 5, 6, 7, 8]. Indeed, while bulk crystals are known to yield plastically via a dislocation multiplication process effective at low-to-intermediate stress (1-100 MPa), decreasing sample size coincides with a gradual strengthening process related to successive changes in terms of plasticity mechanisms including, overall, the lowering of effective dislocation sources activated at larger stress than in bulk [9, 10, 11, 12, 13]. At the nanoscale, the original pristine aspect of nanosized samples constrains dislocations to nucleate at larger stress (>1 GPa) to initiate plasticity. This special kind of deformation is generally called *nucleation-controlled* plasticity in contrast with the well-known *multiplication-controlled* bulk regime.

In 2009, Richter and collaborators used physical vapor deposition to grow for the first time Cu nanowires with diameters as small as 20 nm [14]. These dislocation-scarce nanowires were stressed up to the GPa range (way over the few MPa required to deform bulk Cu) to enable dislocation nucleation and plasticity. The dislocation nucleation process is generally supposed to obey the classical nucleation theory and generally operates from highly-stressed defective regions *i.e.*, the surfaces, edges or corners of nano-objects, leading to the so-called surface dislocation nucleation (SDN) process [15, 16, 17, 18]. So, while it is well known that surfaces play a key role at the nanoscale for functional property applications (*e.g.,* catalysis, adhesion), it becomes obvious that rigorous characterization and optimization of nano-object surfaces are at the heart of nanomechanics and defect engineering.

Nevertheless, the smaller the sample, the more difficult it is to test it mechanically. Since the seminal work of Uchic *et al.* [19], significant efforts have been made to develop micro- and nano-experiments to probe material mechanical behavior at small-scales. Among others, *in situ* tests using transmission (TEM) or scanning (SEM) electron microscopy, on-chip methods and synchrotron X-ray diffraction (Laue or Bragg coherent diffraction imaging) are increasingly used. Ever since, the "smaller is stronger" route was used by hundreds of research groups who performed mechanical tests and simulations on metal micro- and nano-objects (see ref. [10] and references therein). Among others, the studies of Mordehai and collaborators appear as pioneering works when applying such mechanical tests to micro- and nanoparticles

(NPs) using SEM, atomistic and finite-element simulations [20, 21]. Also, Carlton and Ferreira were among the firsts to use diffraction contrast *in situ* TEM nanocompression to study dislocation nucleation in Ag NPs with sizes smaller than 100 nm [22]. A similar approach was used by Issa and collaborators to investigate the mechanical response of MgO ceramic NPs [23, 13]. In particular, the latter study is characterized by quantitative strength discrepancies when comparing experiments to simulations that were recently attributed to surface biases [24].

Indeed, a direct consequence of downsizing is a more and more scattered mechanical response due to both intrinsic and extrinsic experimental biases. Indeed, the yield strength of nano-objects can vary by more than one order of magnitude at constant size as shown *e.g.,* in refs. [25, 26, 27]. Extrinsic biases such as electron-beam irradiation, tip pollution and alignment/contact issues were intensively discussed lately [28, 29, 30, 31, 32] while sample-related intrinsic biases such as shape, chemical effects, surface and pre-existing defects are less well-known. Nonetheless, the dislocation nucleation process itself induces self-stochasticity as being a thermally-activated and probabilistic process *i.e.,* two perfectly same samples and experiments should yield at more or less different strengths. These biases reinforce the data scattering and non-reproducibility of experimental results which are detrimental to in-depth and comprehensive analysis of mechanical properties at small-scales.

In this context, we consider surface roughness as a potential major source for data scattering when considering the measurement of nano-object strength. While Coupeau and collaborators recently highlighted contact reactions between surface steps and dislocations using *in situ* ultra-high vacuum scanning tunnelling microscopy in large-scale sample [33, 34], the surfaces of nano-objects are often rough with surface ledge height ranging from a single atomic layer to several nanometers (see *e.g.*, refs. [35, 36, 21, 37]). This is particularly true for metal or semi-conductor nano-systems while oxide ceramics are known to have sharper and cleaner surfaces. Thus, it is believed that contact singularities gradually act as stress concentrators with decreasing size. Despite its possible influence on the SDN process and strength, this issue has not been addressed comprehensively neither experimentally nor in the simulation of small-scale objects. This is in contrast with the numerous studies performed by tribologists and contact mechanics researchers, at larger scales.

From a theoretical point of view, surface roughness can be described using the power spectrum density of the surface signal and the roughness concepts

developed by Mandelbrot [38]. In this study, we use an approach inspired from the classical roughness theory to design metal NPs with more realistic surfaces using a roughness parameter η, and test the influence of surface roughness on the mechanical properties of NPs using molecular dynamics (MD) nanocompression simulation. We show that surface roughness plays a key role on the strength and elementary deformation processes of metal NPs and propose a model relying on the detailed surface to predict the strength dispersion of NPs under compression accounting for contact roughness.

2. Numerical methods

2.1. Design of nanoparticle with rough surfaces

NPs with rough surfaces are designed using *Pyrough*, an open-source python tool that aims at designing 3D virtual samples (particles, wires, films, *etc.*) with rough surfaces for atomistic and finite-element simulations [39]. *Pyrough* is based on the aforementioned classical roughness theory that provides a mathematical framework for the construction of rough surfaces.
When applied to non-spherical objects, *Pyrough* relies on the sum of cosine functions corresponding to the real part of the Fourier transform of the height distribution auto-correlation function. Each term of the sum allows for the contribution of a given spatial frequency as,

$$h(x,y) = C_1 \sum_{a=-A}^{A} \sum_{b=-B}^{B} G_{a,b}(a^2+b^2)^{-(1+\eta)} cos[2\pi(ax+by)+U_{a,b}] \quad (1)$$

where C_1 is a normalization factor introduced to fit the surface heights to the sample dimensions, a and b are discrete sets of spatial frequencies along x and y (with boundary values $\pm A{=}\pm B{=}\pm 30$), $G_{a,b}$ is a scalar randomly extracted from a reduced centered normal distribution for each (a, b) pair, $(a^2+b^2)^{-(1+\eta)}$ is a function of the power spectrum density that relies on a normalized roughness parameter η (the product $G_{a,b}(a^2{+}b^2)^{-(1+\eta)}$ defines the amplitude of each elementary wave) and $U_{a,b}$ is a random scalar extracted from a uniform distribution on an interval of length π that goes for the cosine's phase. Note that for self-affine surfaces, η is related to the Hurst coefficient H via the relation $\eta{=}(H\text{-}1)/2$.

In this study, we use the *Wulff* module of *Pyrough* with low-index surface energies $\gamma_{\{100\}}$=1296.5 mJ/m^2, $\gamma_{\{110\}}$=1531.2 mJ/m^2 and $\gamma_{\{111\}}$=1196.4 mJ/m^2 (see supplementary information for surface energy calculation details) as inputs to build Au-faceted NPs. Indeed, Au-faceted micro- and NPs have been the subject of a great deal of research recently (see *e.g.,* ref. [20, 21, 40, 41, 42, 43]). In the experiments, they can be built using the dewetting approach where they exhibit surfaces with varying degrees of roughness and no sign of surface oxidation, which makes them the ideal candidate to study the influence of surface roughness under compression at small-scales. Here, Au NPs with height l_0=20 nm are designed for η ranging from 0 to 1 (from the self-affine upper bound to non-stationary configurations) and C_1=0.5 and 1.2. Note that η values were chosen to generate sample surface in qualitative agreement with observations made in nano-metals [35, 36, 21, 37]. Also, C_1=0.5 leads to NPs characterized by surface roughness of a single-layer depth while C_1=1.2 generates coarser surfaces. More details on the design of virtual samples with rough surfaces using *Pyrough* can be found in ref. [39]. Examples of Au NPs (unrelaxed configurations) for various values of η and C_1=0.5 are illustrated in Figure 1a-d. Twenty samples characterized by surfaces with statistically-identical roughness are generated for each (η, C_1) pair. Note that even if several samples have same η and C_1 values, each of them has a unique surface topography due to the randomness induced by $G_{a,b}$ and $U_{a,b}$. Additional samples with flat surfaces are also produced for comparison.

2.2. Molecular dynamics simulation

In the following, atomistic simulations are carried out using the LAMMPS package [44, 45] to investigate the influence of surface roughness on the mechanical behavior of Wulff-shaped Au NPs under displacement-controlled compression. The embedded-atom method (EAM) interatomic potential developed by Grochola et *al.* [46] is used to describe atomic interactions in Au. The transferability of the Grochola potential to nanomechanics is addressed in several studies in which lattice, surface and dislocation properties are shown to accurately reproduce experiments and DFT results [47, 48, 20, 49, 50, 51]. A timestep of 2 fs is used for all MD simulations.

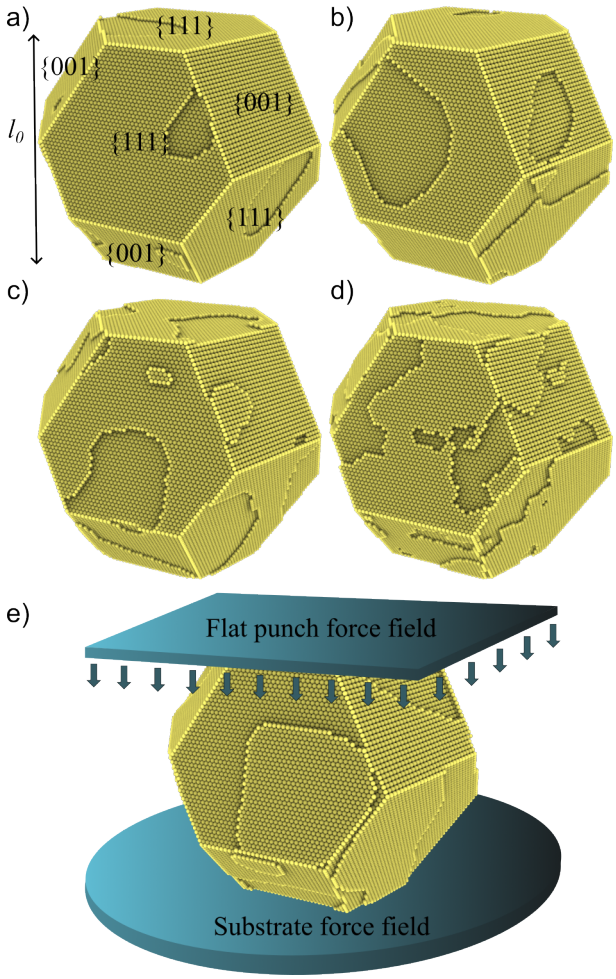

Figure 1: Wulff-shaped Au nanoparticles with rough surfaces as generated using *Pyrough* (unrelaxed configurations), a) η=0.95, b) η=0.75, c) η=0.25, and d) η=0, f) the nanocompression simulation setup is made of two axis-aligned and infinite force fields that behave as indenter and substrate, respectively.

2.2.1. Sample equilibration

Designing samples with *Pyrough* leads to a mathematically-defined surface roughness that does not necessarily correspond to the thermodynamics equilibrium. After processing with *Pyrough*, as-cast samples are subjected to a rigorous equilibration procedure in order to prevent non-physical surface ledges from influencing the mechanical response during nanocompression. To optimize the sample surface, the potential energy is initially minimized at 0

K using the conjugate gradient and the FIRE algorithms [52] consecutively with a convergence criterion on the force norm (f_{norm}=10^{-8} eV.Å^{-1}). Then, a thermal equilibration procedure using shrink-wrapped non-periodic boundary conditions is performed as follows: 1) the sample is first subjected to an initial 10 ps run in the NVE ensemble to initialize atom velocities and temperature (10 K target temperature), 2) a temperature ramp is ran over 20 ps in the NVT ensemble up to *c.a.* 810 K corresponding to 70% of the theoretical melting temperature of Au, 3) a high-temperature equilibration run is performed during 1 ns at constant temperature, 4) the sample is quenched down to 300 or 10 K (for later compression purpose) where a final equilibration run is performed during 0.5 ns.
The mean square displacement (MSD) of the atoms is computed to monitor the reconstruction of rough surfaces during the whole equilibration process. The MSD tracks the deviation of atomic positions $\mathbf{r_i}(t)$ over time with respect to a reference $\mathbf{r_i}(0)$.

$$\langle r^2(t)\rangle = \frac{1}{N}\sum_{i}^{N} |\mathbf{r_i}(t) - \mathbf{r_i}(0)|^2 \tag{2}$$

where N is the total number of atoms. It is worth mentioning that while such a rigorous equilibration process approach relaxes mathematically-constructed surfaces, larger-timescale surface diffusion is not modeled during the following nanocompression simulations. While enhanced in very small NPs (sub-10 nm) [53, 54], we believe that this effect should not quantitatively impact the larger systems (NPs of tens to hundreds of nanometers) this study aims to describe.

2.2.2. Nanocompression

MD nanocompression simulations along the z=[111] direction perpendicular to the NP top surface are performed at room temperature using the Nosé–Hoover thermostat and shrink-wrapped non-periodic boundary conditions following the methodology introduced in refs. [23, 55]. Additional simulations are also performed at T=10 K to reduce the thermal noise while characterizing deformation processes. In a nutshell, two axis-aligned, infinite and flat repulsive force fields which model a flat punch indenter and a substrate are used respectively to deform and sustain the NP as shown in Figure 1e. Indenter and substrate force fields are modeled by $F_{ff} = -\sum_i K(z_i - z_{ff})^2$ where K is the force field constant, z_{ff} and z_i are the z-coordinates of the

force-field and i^{th} atom, respectively. While the influence of K on the mechanical response of rounded NPs was recently discussed in the literature [56], here we use K=1000 eV.Å^{-3} large enough to reduce the penetration of the indenters in flat and rough NPs (as usually done in experiments). To model uniaxial compression, the indenter force field is moved downwards against the NP while the substrate force field is maintained at a fixed position during the whole nanocompression simulation. The top indenter is displacement-controlled with a rate equivalent to a constant strain rate of 10^8 s^{-1}, typical of MD simulations. The load is defined as the force exerted by the indenter while displacement δ=$l_0 - l$ is computed as the variation of the maximum NP height during the simulation.

The contact surface definition requires a specific treatment in case of rough surfaces due to its intrinsic discontinuous nature. Here we use an approach inspired from the work of Goryaeva *et al.* [57], *i.e.* a criterion $|z_{ind} - z_i|$<1 Å (with z_{ind} the indenter position) is used to identify the group of atoms that contact with the indenter *on-the-fly* during the simulation. Thus, the contact surface S is computed using a geometrical factor associated to the $\{111\}$ surface as $S = n_i.\frac{{a_0}^2\sqrt{3}}{4}$ where a_0=4.08 Å is the lattice parameter of Au and n_i is the total number of atoms contained in the group. This method is used to get rid of outlier results provided by regular convex contour methods (*e.g.,* Delaunay triangulation) in case of distinct top islets of atoms related to surface roughness [58]. Note that the definition of contact in case of rough surfaces is still widely debated in the literature (see *e.g.*, ref. [59]).

During nanocompression, the components of the stress per atom tensor are computed using the Virial theorem,

$$\sigma^i_{\alpha\beta} = -\frac{1}{V_i}\left[m_i v^i_\alpha v^i_\beta + \frac{1}{2}\sum_j r^j_\alpha f^{ij}_\beta\right] \tag{3}$$

where v^i_α and v^i_β are the velocities of atom i along α and β directions, m_i is the mass, r^j_α is the position of nearby atom j along the α direction and f^{ij}_α is the force exerted by the neighbor atom j on atom i along the β direction. The atomic volume V_i is computed using the VORO++ Voronoi tessellation approach [60]. Due to the inconsistency of V_i for surface atoms, the stress per atom is computed for non-surface atoms only. The resolved shear stress per atom τ^i_s in slip system s is computed using the Schmid law,

$$\tau^i_s = (\sigma^{\mathbf{i}} \cdot \mathbf{n_s}) \cdot \mathbf{b_s} \tag{4}$$

where $\mathbf{n_s}$ is the slip plane normal and $\mathbf{b_s}$ is the shear direction.
The per-atom von Mises stress is computed as,

$$\sigma_M^i = \frac{1}{\sqrt{2}}\Big[\left(\sigma_{xx}^i - \sigma_{yy}^i\right)^2 + \left(\sigma_{yy}^i - \sigma_{zz}^i\right)^2 + \left(\sigma_{zz}^i - \sigma_{xx}^i\right)^2 + 6\left((\sigma_{xy}^i)^2 + (\sigma_{xz}^i)^2 + (\sigma_{yz}^i)^2\right)\Big]^{1/2} \tag{5}$$

Atomic configurations are characterized using the polyhedral template matching (PTM) method [61] and the dislocation extraction algorithm (DXA) [62] as implemented in the Ovito software [63].

3. Results

3.1. Sample equilibration

Figure 2a illustrates an example of MSD evolution during sample equilibration for a gold NP characterised by η=0.0 and C_1=0.5 (one-layer depth surface roughness). Results show a typical first-order system evolution with the MSD increasing up to a steady-state. In the high-temperature equilibration regime, such a behaviour can be modeled using a first-order approach $\langle r^2(t)\rangle = K(1 - e^{-\frac{t}{\tau}})$, where K and τ are the system gain and time constants, respectively. The equilibration time $t_{equi}=3\tau$ is defined as the time to reach 95% of the MSD final value. Please note that η=0 corresponds to the self-affine upper bound (H=1) that already generates significantly rough surfaces. Thus, the rest of the study will rather focus on less-rough non-stationary surfaces (η>0). t_{equi} for η ranging from 0 to 1 and NPs with flat surfaces are illustrated in Figure 2b. While each NP is characterised by a unique (K, τ, t_{equi}) triplet, a clear trend emerges for t_{equi}: the rougher the NP, the longer t_{equi}. Such a tendency relies on the topography of the surface height distribution $h(x, y)$. Rougher surfaces (low η) are characterized by a larger contribution of high-frequency components of $h(x, y)$ that induce energetically unfavorable configurations such as *zig-zag* surface terraces or small atomic islets, as shown in Figure 1c and d. During equilibration, terraces become more regular and originally-isolated islets either merge with adjacent surface steps or undergo reshaping in preferred directions, what requires a longer equilibration time. For less rough samples (larger η), surfaces primarily feature extended and steadier atomic terraces, as shown in Figure 1a. Thus, the equilibration process essentially involves the smooth and quick

reorientation of surface steps. For NPs with originally perfectly flat surfaces, t_{equi} is almost zero as Wulff-shaped NPs are already close to their equilibrium shape before the simulation.

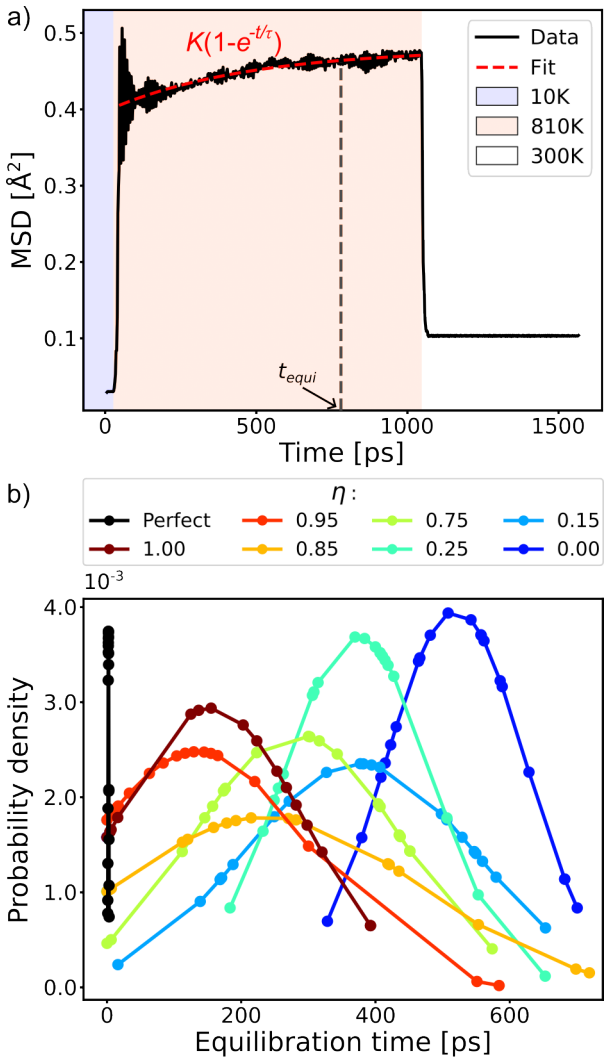

Figure 2: Thermal equilibration of Au-faceted nanoparticles with rough surfaces, a) Evolution of the MSD during sample equilibration for a nanoparticle characterised by (η=0.00, C_1=0.5), b) Equilibration time t_{equi} distribution as a function of the roughness exponent η, for scaling coefficient C_1= 0.5. 20 samples (symbols) are tested for each η while curves are guides for the eyes. For the perfect case (nanoparticle with flat surfaces), the probability density function is reduced by a factor of 190 to scale with the other distributions.

The reorganization of surface atoms during thermal equilibration induces a variation of the height distribution morphology of the NP surface. Figure 3 shows the variation of the apparent roughness exponent before and after equilibration, respectively η_0 and η_{eq}, for the whole (η, C_1=0.5) samples collection, both computed using *Pyrough* -surface option applied to the atomic configuration. Note that η_0 might slightly differ from *Pyrough*'s input η as it is computed from the sample's top surface that is restricted by a discrete set of atomic positions while η relies on the numerical surface $h(x, y)$ defined by Equation 1. Finally, results show that η_{eq}/η_0 is slightly larger than 1 in most of the cases meaning that the sample equilibration smooths the height distribution $h(x, y)$ without completely cancelling the surface roughness. Also, the spread of the η_{eq}/η_0 distribution increases as η decreases in agreement with our prior observations wherein a significantly larger number of atoms is displaced (larger MSD) when increasing the surface roughness.

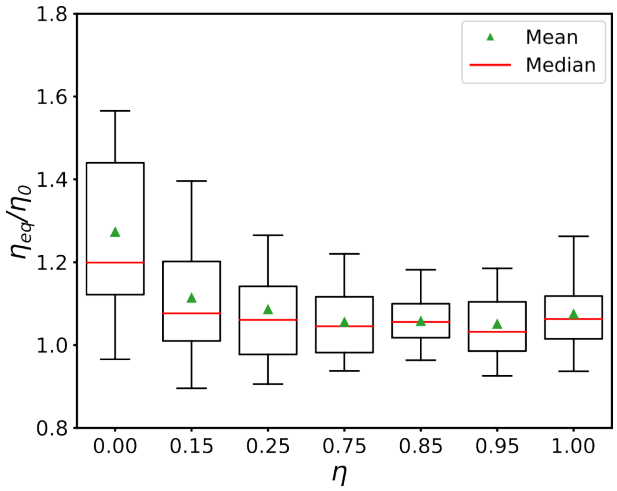

Figure 3: Evolution of the normalized roughness exponent η_{eq}/η_0 after/before sample thermal equilibration as function of input η. The box plot relies on the central 50% of the sampling while bars show the scatter of the last 50%.

3.2. Mechanical response

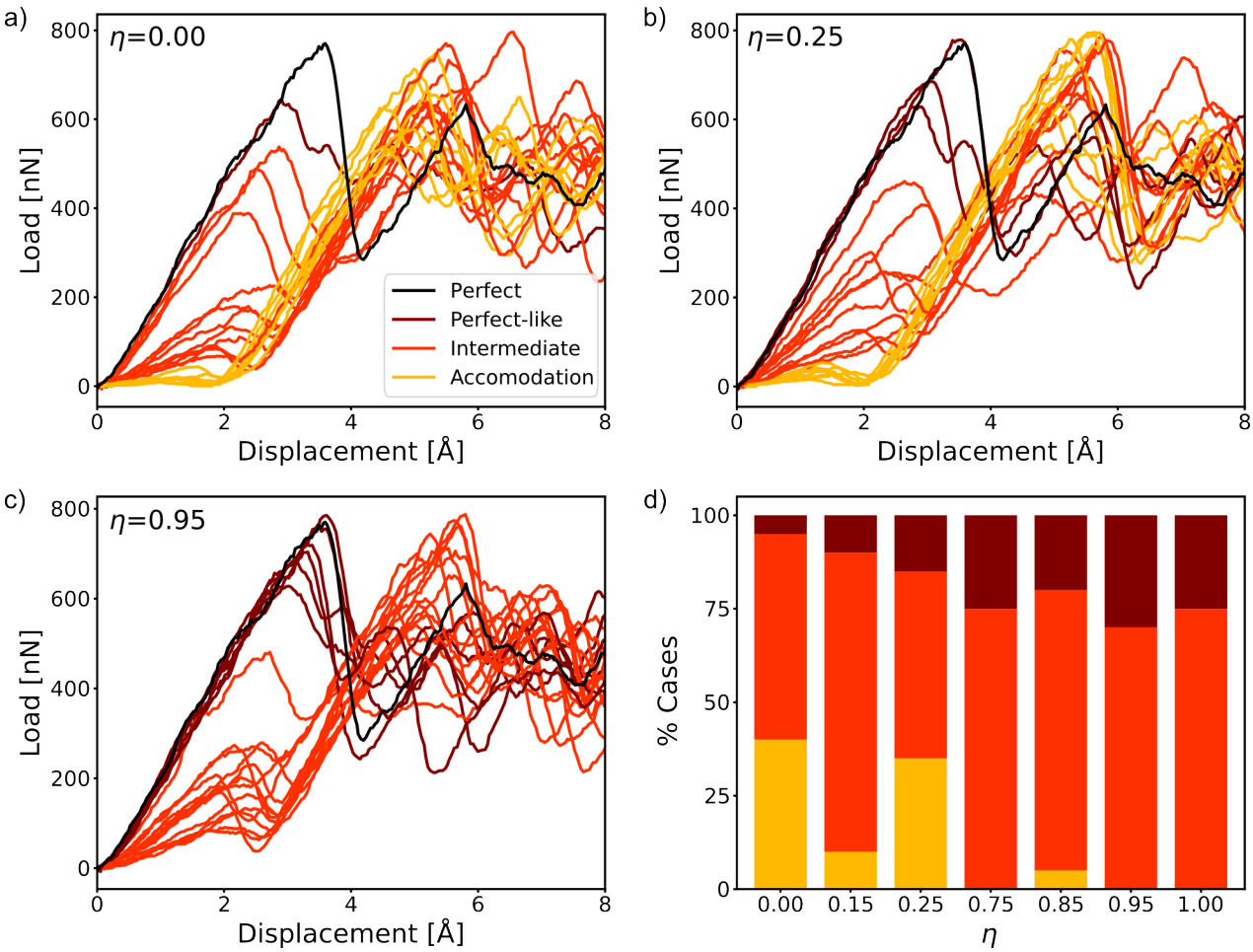

Figure 4: Load-displacement for <111>-oriented Au-faceted nanoparticles with rough surfaces compressed at T=300 K, a) η = 0.00, b) η = 0.25, and c) η = 0.95. 20 samples are tested for each (η, C_1=0.5) configuration. *Perfect-like*, *intermediate* and *accommodation* cases are illustrated in brown, red and orange respectively while the *perfect* case (nanoparticle with flat surfaces) is shown in black, d) Sample fraction distribution among the *Perfect-like*, *intermediate* and *accommodation* cases as a function of η.

Figure 4 illustrates the mechanical response of Au-faceted NPs compressed along [111] using MD at T=300 K for various level of surface roughness as compared to one of the perfect case. For the sake of clarity, data are filtered using the Savitzky-Golay method (filter window f_w=7, polynomial order n=1) that allows to get rid of temperature-induced fluctuations

[64]. The two usual elastic and plastic regimes of deformation are easily recognizable in the case of the NP with perfectly flat surfaces (*perfect* case). They are delimited by a yield force of F_y^p=779 nN, where a load drop marks the beginning of the plastic deformation regime. Afterwards, the mechanical test consists in a succession of quasi-linear elastic reloads followed by force drops that highlight each plastic event. The mechanical response of NPs with rough surfaces is significantly different from the one of the *perfect* case. In the following, it is rationalized into three categories, *i.e.* the *perfect-like*, the *intermediate* and the *accommodation* cases, that progressively emphasize the impact of surface roughness. The *perfect-like* behavior is characterized by an initial response particularly close to the one of the *perfect* case in the elastic regime. However, the first load drops occur at slightly lower critical displacement δ_y and force F_y, the latter ranging from $0.8F_y^p$ up to F_y^p. In this regime, secondary force peaks are of lower amplitude when compared to the *perfect* case. Also, the *intermediate* trend is characterized by various load-displacement slopes in the elastic regime all below the one of the *perfect* case including F_y in the $\left[0.2F_y^p : 0.8F_y^p\right]$ range. While first force drops are of lower amplitude and occur for lower δ_y, secondary elastic reloads can reach particularly high maximum forces. Finally, *accommodation* cases are characterized by an initial pseudo-contact with almost zero force recorded until the displacement reaches $\sim$2 Å, where the force starts to increase. This particular trend is observed when the top surface of the NP is characterized by one or several small atomic islets (made of a few atoms each) that are pushed by the indenter below the surface of the NP with little effort. The critical displacement of about $\sim$2 Å does not depend on η but is rather imposed by the displacement at which the indenter starts to deform subsurface atomic layers. This distance can be approximated by the $\{111\}$ interplanar distance $d_{\{111\}}=a_0/\sqrt{3}$=2.36 Å. One can note that in this case there is no clear evidence of elastic deformation of the subsurface layers during the pushing of the surface atomic islets within the NP subsurface region. This process that heals the surface in case of 1-layer surface roughness (C_1=0.5) is further illustrated in the supplementary information (Figure S1). As shown in Figure 4, the second load peaks consecutive to the first dislocation nucleation event can reach a fraction of F_y^p whatever the case. A detailed analysis of secondary peaks as a function of the roughness parameter is provided as supplementary information (Figure S2). While secondary peaks can increase again beyond first load maxima, they remain significantly lower than F_y^p whatever the roughness confirming the important role of roughness. In the

experiments, load-controlled tests are constrained by maximum loads which are shown here to be impacted by the surface roughness due to the irreversible character of plastic deformation. It is worth noticing that, at variance with load-controlled tests, displacement-controlled tests allow to identify each load drop independent of its amplitude.
The fraction of *perfect-like*, *intermediate* and *accommodation* cases for η ranging from 0 to 1 are depicted in Figure 4d. *Intermediate* cases are the most observed on the whole η range. *Accommodation* cases are more prevalent for lower η values as more roughness favours surface islets but fully disappear for η>0.85 where *intermediate* cases are mostly present, followed by *perfect-like* cases, the proportion of which increases while decreasing the surface roughness.

3.3. Deformation processes

As previously shown, surface roughness can drastically reduce the critical force at which metallic NPs yield. Indeed, surface terraces act as stress concentrators from which dislocation nucleate when the yield force is reached. This process is illustrated in Figure 5 where the von Mises stress per atom σ_M^i is emphasized just before the first plastic event happens in (i) a NP with flat surfaces and (ii) a (η=0.85, C_1=0.5) NP characterized by a load-displacement curve with the *intermediate* trend. For the flat-surface NP, σ_M^i spatial distribution is characterized by a lens-shaped symmetrical pattern right beneath the (111) top facet (similar to those shown in refs. [20, 65, 66]) and a maximum value of about 8.64 GPa is measured close to an external vertex, at 8.5 Å under the top surface. For the NP with rough surfaces, the stress pattern is more asymmetric as following the rough surface topography and is localized right beneath a surface step. Also, the stress maximum (∼8.56 GPa) is close but slightly lower than the one measured in the flat NP. Figure 5 also emphasizes the lack of stress concentration in the vicinity of lateral facets (besides the lateral surface steps) leading to an incipient plasticization process mainly confined below the contacting surface, where the external load is applied.

The Figure 6 illustrates an example of a first plastic event characterized in a (η=0.25, C_1=0.5) NP, *intermediate* load-displacement trend. In this case, a dislocation dissociated in the $(\bar{1}\bar{1}1)$ plane nucleates at a critical displacement δ_y= 1.93 Å from a one-layer height atomic terrace that emerges

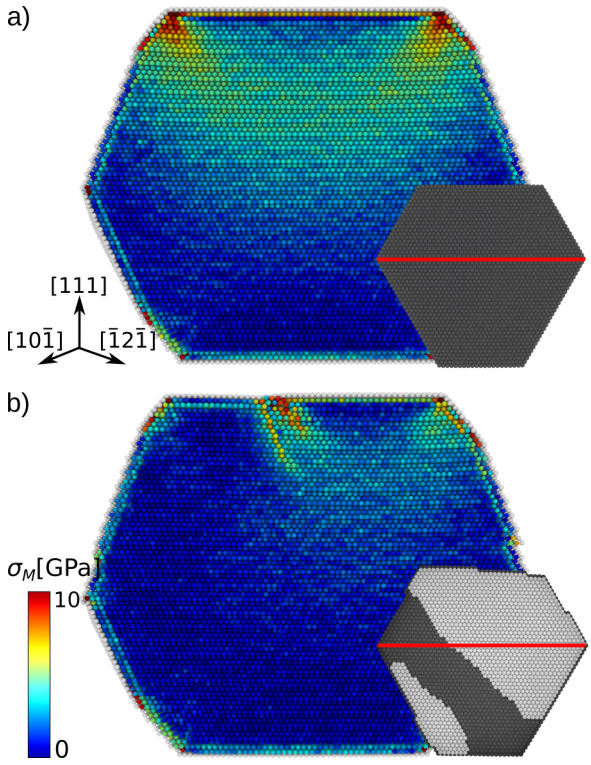

Figure 5: Per atom von Mises stress stress σ_M^i in Au-faceted nanoparticles under compression at T=10 K, cross-section view. Snapshots were taken ahead of the the first dislocation nucleation event in a) a nanoparticle with flat surfaces (*perfect* case) and b) a nanoparticle with rough surfaces (η=0.85, C_1=0.5), *intermediate* case. Insets illustrate the nanoparticle top surface where first-layer atoms are colored lighter than those below. Red lines illustrate main figure cross-section.

at the edges of lateral facets (Figure 6a, c① and c②). The dislocation is made of a leading $\frac{1}{6}[1\bar{2}\bar{1}](\bar{1}\bar{1}1)$ and a trailing $\frac{1}{6}[\bar{1}\bar{1}\bar{2}](\bar{1}\bar{1}1)$ Shockley partial dislocations separated by an intrinsic stacking-fault. After nucleation, the dislocation starts gliding through the NP while its emerging screw components shear the NP surface zipping up the surface step (Figure 6 insets). This process contributes to the reduction of the NP's height and, consequently, to the load decrease, conditioned by the displacement-controlled character of the simulation, shown in Figure 6b up to a displacement of about 3.34 Å. Concurrently, a significant increase of the NP top surface area S from 47.6 nm^2 up to 132.4 nm^2 is noticed. At this stage, S closely approaches the area of a perfectly-flat NP top facet *c.a.* S^p=133.6 nm^2, which confirms that first

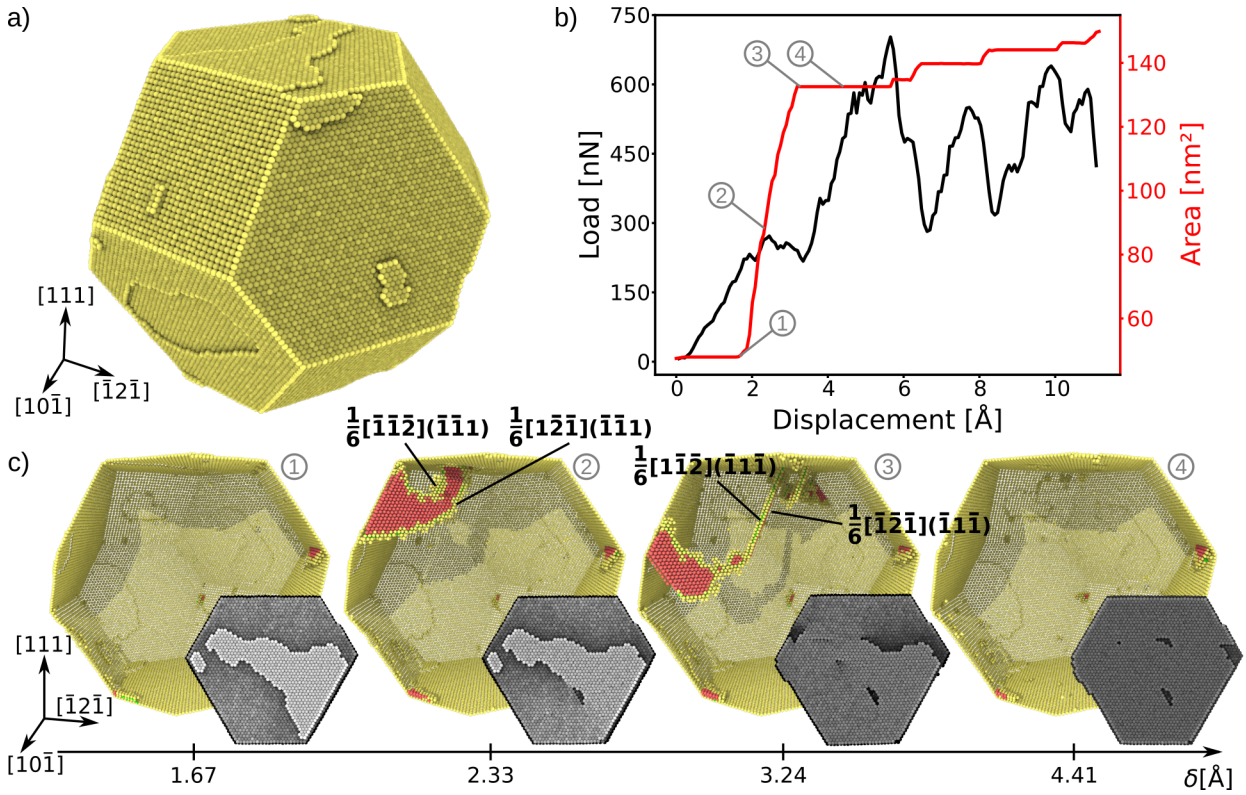

Figure 6: Dislocation nucleation in a Au-faceted NP with rough surfaces (η=0.25, C_1=0.5) under compression at T=300 K. a) initial sample (after equilibration), b) load-displacement curve and top surface area evolution, c) dislocation nucleation process for displacements between 1.67 and 4.41 Å. Surface and partial dislocation core atoms are colored in yellow, atoms in the stacking-fault are colored in red. Perfect crystal atoms are removed for the sake of clarity. Insets show the evolution of the top surface ledges during the dislocation nucleation/propagation process.

plastic events mostly cancel one-layer surface steps resulting in a configuration akin to the *perfect* case. This justifies the particularly-high amplitude of the second force peaks shown in Figure 6b, close to the *perfect* case yield force (F_y=703 nN, *c.a.* $0.9F_y^p$). One can note that the emerging components of the dislocation strictly follow the surface step during the shearing process which implies the cross-slip of a portion of the dislocation into the ($\bar{1}1\bar{1}$) plane, as shown in Figure 6c③.

However, cross-slip is not the sole original dislocation process influenced

by surface roughness. Figure 7 depicts the first dislocation nucleation process in a (η=0.75, C_1=0.5) NP (*intermediate* load-displacement trend). Here, we look at the dislocation nucleation process from the inside of the NP from where surface steps oriented along the $[0\bar{1}1]$, $[10\bar{1}]$, $[1\bar{1}0]$ and $[2\bar{1}\bar{1}]$ directions are identified. While the yield of the NP is characterized by the nucleation of regular 1/2<110>{111} dislocations (colored in green), one can also identify dislocation nucleation in the {001} crystallographic planes (colored in blue). This is for example the case in Figures 7e,f where a $1/2[\bar{1}0\bar{1}](0\bar{1}0)$ dislocation nucleates after a short period during which two 1/2<110>{111} dislocations were pinned at the ends of a $[2\bar{1}\bar{1}]$-oriented surface step. These new dislocations have 1/2<110> Burgers vectors and are only observed in the cases of rough surface NPs accommodating both particular ledge directions and stress field. Finally, one can notice that, again in this case, the nucleation of the various dislocations allows the withdrawal of the original one-layer surface steps, at the top of the NP.

4. Discussion

Surface roughness influences both the mechanical response of nanocrystals and their relative elementary deformation processes. As shown in Figure 6, single-layer surface steps drastically reduce the yield force F_y of Au-faceted NPs while changing dislocation nucleation centre locations from NP top surface edges to ledges. It is well-known that dislocation plasticity is a dissipative process and, here, the energy drop computed during the first dislocation nucleation event is lower in amplitude in case of NPs with rough surfaces when compared to the perfect case (see supplementary information). We believe that the relative difference in energy dissipation is due to the surface ledge correction in case of rough surface NPs as compared to the creation of fresh surface steps in originally pristine NPs. These observations corroborate previous results on the influence of surface steps on the dislocation nucleation process for which various models can be found in refs. [67, 68, 69, 70].
The gradual disappearance of surface steps while dislocations nucleate and the features of the first dislocations are closely related, with the top surface height morphology driving the original type of defect that nucleates and its motion. Indeed, we observed that dislocations can change their original glide direction and slip plane as following the surface topography via the cross-slip of screw dislocation portions, below the surface. This process can

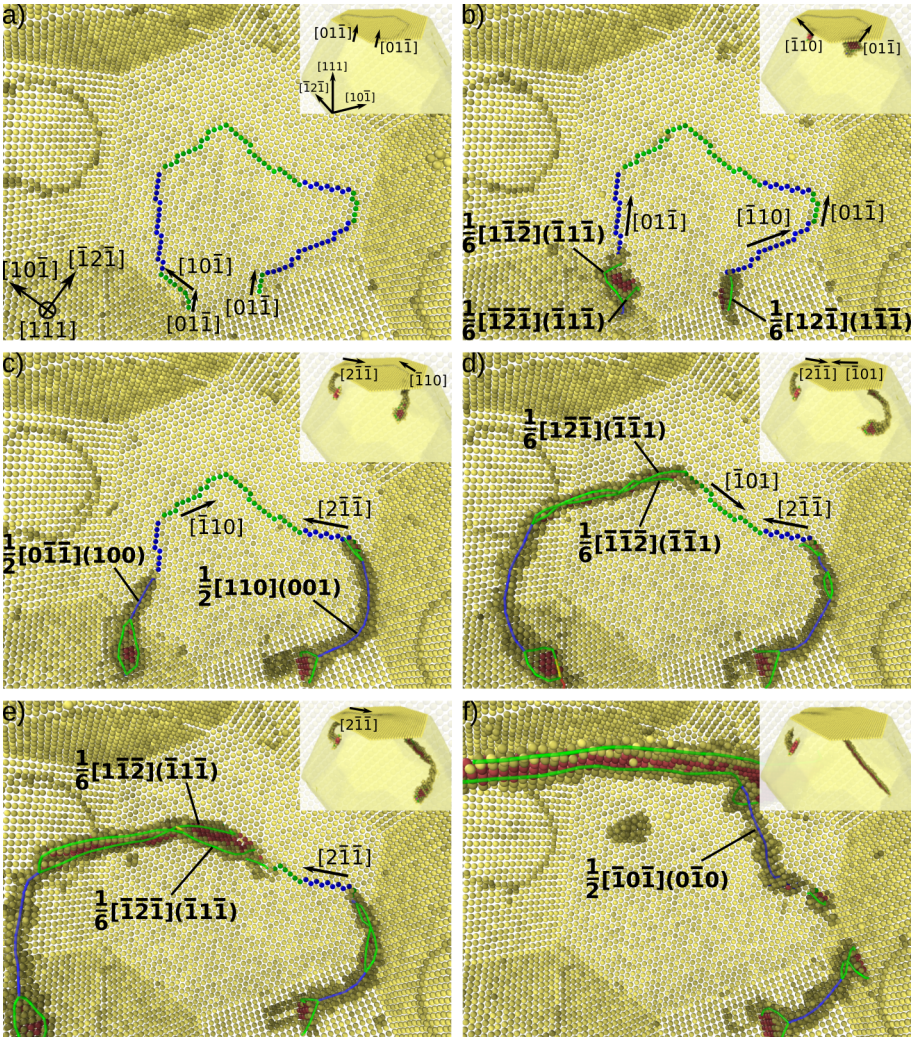

Figure 7: Dislocation nucleation in a Au-faceted NP with rough surfaces (η=0.75, C_1=0.5) under compression at T=300 K, a) δ=3.63 Å, b) δ=4.18 Å, c) δ=4.74 Å, d) δ=5.19 Å, e) δ=5.58 Å and f) δ=6.97 Å. View from the inside of the nanoparticle from which perfect crystal atoms are removed for the sake of clarity. Dislocations in {111} and {001} slip planes are colored in green and blue, respectively. Same colors are used to identify corresponding surface steps.

lead to anomalous slip as, *e.g.* in uncommon 1/2<110>{001} slip systems (see Figure 7), in a similar manner to what was recently observed in diffraction experiments performed on platinum NPs [71]. While such a peculiar behaviour is the result of a complex combination of surface step direction,

primary *vs.* cross-slip planes, Burgers vectors and local stress, one can note that a simple Schmid factor analysis also corroborates the results. A particularly high Schmid factor (m=0.47) exists in the $1/2[0\bar{1}\bar{1}](100)$ slip system (see Figure 7c) while the maximum Schmid factor for a 1/6<112>{111} under compression along [111] is m=0.31.

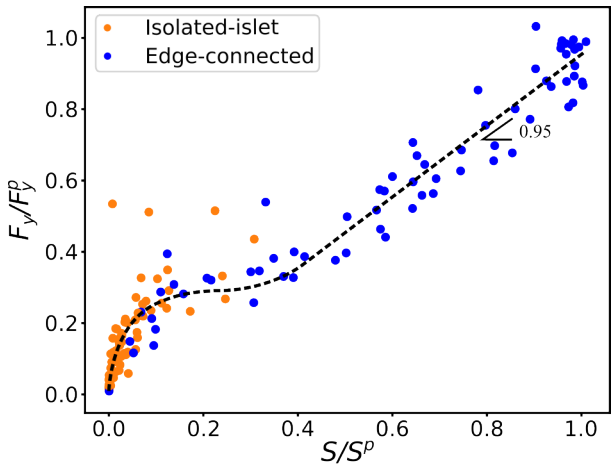

Figure 8: Rough surface nanoparticle yield force F_y *vs.* (initial) top surface area S, both respectively normalized by mean F_y^p and S^p associated to flat-surface NPs. Blue symbols: edge-connected top surface cases, orange symbols: isolated-islet cases. The dashed curve emphasizes the F_y/F_y^p trend (guide for the eye).

The main objective of this study is to quantify the impact of surface roughness on the critical strength of metal NPs. In this context, while load *vs.* displacement is the raw data for both the numerical and experimental nanomechanics communities, the stress definition remains crucial. As a consequence, two definitions relying on the perfectly flat surface S^p (that can easily be retrieved in an experiment) and on the rough one S, respectively the apparent and real compressive stresses, are used in the following. Figure 8 illustrates the variations of the yield force F_y of NPs with rough surfaces as a function of the initial contact surface S (critical real stress σ_y=F_y/S), both respectively normalized by F_y^p and S^p, mean data derived from the NPs with flat surfaces (*perfect* case). One can easily identify two regimes from the data set that are independent from η: 1) for larger S/S^p, F_y/F_y^p follows a linear trend with fairly low dispersion and a slope near to 1 and 2) for S/S^p lower than 0.4, variations are non-linear. F_y/F_y^p first increases drastically before

the slope reduces and returns to the linear regime described above. A more detailed analysis of the contact surfaces shows that the F_y/F_y^p two-regimes trend is due to the propensity of surface top layers to be connected (or not) to a lateral edge. Thus, two cases are identified and illustrated in Figure 9a and b. On the one hand, the top layer is fully disconnected from the lateral surface (Figure 9a) leading to the formation of one or few *isolated-islets* of atoms. On the other hand, the top layer is connected to a lateral facet via an edge (Figure 9b) and we call this configuration *edge-connected* in the following. Note that samples characterized by top surface isolated-islets and edge-connected surfaces are plotted in orange and blue, respectively, in the Figure 8. Adjusting the corresponding data using a least squares fitting procedure [72], a linear dependency of the edge-connected dataset with a slope of 0.95 is confirmed. While the isolated-islet dataset shows a more complex dependency on S/S^p, it is characterized by a slope of 2.08 when relying on the same linear fit. In both regimes, the critical force F_y to nucleate first dislocations scales with the evolution of the contact surface area S imposed by the first-top layer and η, without changes in the critical (real) compressive stress σ_y or shear stress τ_y. Nevertheless, the slope variation emphasizes an evolution of the dislocation nucleation process. On the one hand, the dislocation nucleus has a half-loop shape when nucleating from an isolated islet, for low S/S^p, as illustrated in Figure 9a,c. Otherwise, in case of edge-connected (large S/S^p), the nucleation centres are always located nearby a lateral edge. Consequently, dislocation nuclei in this case have one tip lying on a lateral facet while the second one is attached to the rough top surface. Such a configuration leads to the nucleation of a quarter-loop dislocation as shown *e.g.*, Figure 9b,d. This process is particularly similar to the one occuring in flat-surface NPs. No significant differences in terms of dislocation radii were noticed with *e.g.,* $r_{1/4}$=9.18 Å and $r_{1/2}$=9.24 Å for the two dislocations illustrated in Figure 9, respectively. Also, maximum shear stresses are particularly close in the both cases *c.a.* 6.18 GPa (isolated-islet case) and 6.09 GPa (connected-edge case).

Several studies focusing on the nanocompression of Au-faceted NPs with perfectly flat surfaces illustrate the nucleation of dislocation quarter-loops that further extend during compression [21, 73, 51]. Owing the dislocation shapes (quarter- *vs.* half-loop) observed here and the force increase of about a factor of 2 between the two regimes while showing particularly close critical dislocation radii, we believe that the yield-force trend computed in the isolated-islet regime is related to step and dislocation size effects.

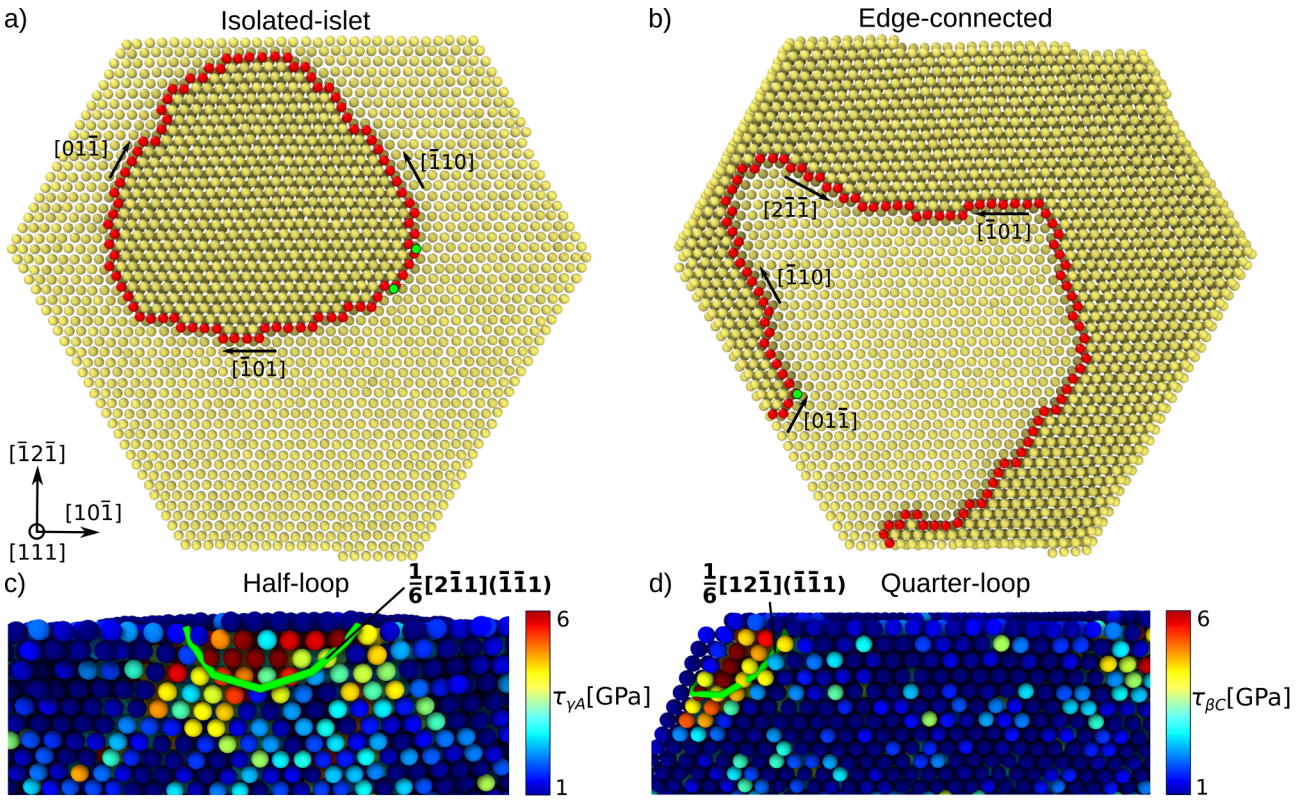

Figure 9: Influence of the contact surface configuration (isolated-islet or edge-connected) on the dislocation nucleation process, a,b) contact surface: a) isolated-islet and b) edge-connected configurations, top view. Surface step atoms are highlighted in red and green dots emphasize dislocation nucleation emerging segment locations, c,d) shear stress per atom computed in the partial slip system in which the first Shockley partial dislocation nucleates. Cross-section view normal to the slip plane identified using the Thomson tetrahedron notation. The atomic configuration is captured few steps before the first plastic event, while the latter critical dislocation configuration (colored in green) that corresponds respectively to c) an half- and d) a quarter-loop, is superimposed for the sake of clarity.

Consequently, η impacts dramatically the yield force F_y but only weakly the critical real stress σ_y as soon as it is defined using the detailed contact surface S *i.e.,* the one that accounts for isolated-islets and connected-edge domains. Nevertheless, such a detailed description of S is generally not accounted in nanomechanical experiments that usually rely on apparent flat surfaces (that we approximate here to S^p), due to insufficient resolution or

2D projections. In these conditions, the critical apparent stress measured in the experiment σ_y^*=F_y/S^p is directly impacted by the surface roughness. To propose a predictive model of σ_y^*, one can define the contact surface fraction ϕ=S/S^p. Whereas ϕ can be retrieved using atomic force microscopy in the experiment, it is computed here using $h(x, y)$ as,

$$\phi = \frac{1}{S^p} \iint h(x,y) \cdot \theta \left[h(x,y) - (h_{max} - h_{cut}) \right] dx.dy \tag{6}$$

where h_{max} is the maximum value of the height distribution, h_{cut} is a cut-off distance imposed here as half the {111} interplanar distance (h_{cut}=1.18 Å) and θ is the Heaviside step function defined as $\theta(\lambda) = 0$ if $\lambda < 0$ and $\theta(\lambda) = 1$ if $\lambda \geq 0$. Owing the sole critical compressive stress σ_y^p in the case of a perfectly flat NPs, the critical apparent stress is defined as,

$$\sigma_y^* = \chi.\phi.\sigma_y^p \tag{7}$$

with χ a contact shape factor equal to 1 (edge-connected case) or 2 (isolated-islet case) and σ_y^p=6.20 GPa is averaged over the 20 compression tests modeled using a perfectly-flat NP. Note that this latter can also be retrieved from nanocompression experiments or from theory.

In Figure 10, the σ_y^* model relies on the whole set of height distribution $h(x, y)$ used in the MD nanocompression simulations described in the previous section. Results show that model σ_y^*/σ_y^p compares with a satisfactory agreement with data extracted from MD nanocompression simulations and both are characterized by the similar tendency, *i.e.* the rougher, the weaker. Note that minor discrepancies still exist. We believe that they could be related to surface topological details, such as the surface step orientation and density, and temperature-induced stochastic effects. Mean μ and standard deviation s of σ_y^*/σ_y^p distribution for simulation and model are presented in Table 1 as a function of the roughness exponent. While the *perfect* case is characterized by a particularly narrow distribution centered around σ_y^*/σ_y^p=1, samples with rough surfaces show wider distributions shifted towards lower σ_y^*/σ_y^p. Extreme cases η=0.0 and η=0.25 show distributions centered around extreme low $0.22\sigma_y^*/\sigma_y^p$ and $0.32\sigma_y^*/\sigma_y^p$, respectively. One can note that a significant downgrade of NP strength is still noticed in the smoothest cases (see *e.g.*, η=0.95 and η=1), with statistical distributions centered around $\sim 0.50\sigma_y^*/\sigma_y^p$. This confirms that even fairly-low surface roughness induces

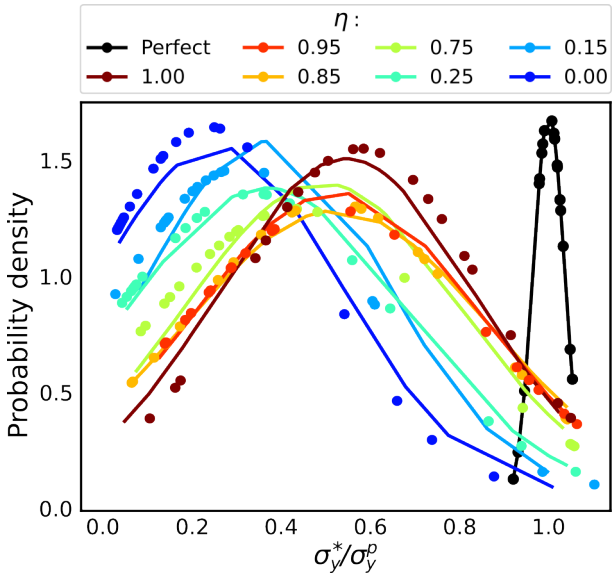

Figure 10: Critical apparent stress σ_y^* distribution normalized by the perfect case yield strength σ_y^p as a function of η. Symbols: MD simulations, curves: model (Equation 7). For the sake of the scaling, the probability density function of the *perfect* case is reduced by a factor of 6.67.

large critical stress variations when compared to the perfect case, with a decrease that can reach up to 90% of σ_y^p. Finally, the abrupt transition from a narrow to a widespread critical strength distribution confirms that roughness is the source of significant dispersion of the measurements (way over temperature fluctuations) whatever its level.

While investigating the mechanical response of rough surface NPs (Figure 4), we observed that secondary force peaks were in the same range as the *perfect* case primary's and this result was attributed to a resorption process of the single-layer surface step induced by the nucleation and propagation of the first dislocations which made the NP pristine again. To investigate further the influence of surface roughness, additional simulations involving larger height distributions (see Figure 11a) are presented in the following with NPs population characterized by C_1=1.2 and same η range. Figure 11 summarizes the simulation results where *intermediate* and *accommodation* cases can still be observed (as in the single-layer surface step case) at variance with the *perfect-like* regime. This behaviour is due to the larger amplitude

Table 1: Mean μ and standard deviation s of σ_y^*/σ_y^p distributions obtained by MD simulations (μ_S and s_S) and model Equation 7 (μ_M and s_M).

		η						
		0.00	0.15	0.25	0.75	0.85	0.95	1.00
$C_1 = 0.5$	μ_S	0.22	0.29	0.32	0.41	0.49	0.49	0.56
	μ_M	0.24	0.34	0.34	0.47	0.50	0.50	0.52
	s_S	0.25	0.29	0.31	0.33	0.32	0.33	0.27
	s_M	0.27	0.27	0.31	0.31	0.34	0.32	0.28
$C_1 = 1.2$	μ_S	0.10	0.12	0.12	0.19	0.17	0.24	0.22
	μ_M	0.11	0.13	0.13	0.20	0.18	0.27	0.21
	s_S	0.09	0.11	0.12	0.15	0.16	0.21	0.16
	s_M	0.08	0.11	0.12	0.15	0.15	0.20	0.17

of $h(x, y)$ which favors smaller contact surface areas and thus, an even more pronounced effect of roughness on the mechanical response as confirmed by the shift of σ_y^*/σ_y^p distributions towards lower values (Figure 11c, Table 1). Also, secondary load peaks illustrated in Figure 11b are of lower amplitude, *i.e.* they mostly reach intermediate values below primary force peaks, as another consequence of C_1 variation. The evolution of the dislocation behavior under the indenter is also influenced by the presence of numerous surface steps and terraces at various heights. While dislocations nucleate from primary surface steps as in the C_1=0.5 case, they latter interact with subsequent steps originally located in the underlying atomic layers. As illustrated in Figure 12, several scenarios emerge including: i) neighboring atomic step serving as anchor points for dislocations that impede locally the dislocation microstructure growth during compression while promoting the nucleation of dislocation from other locations (Figure 12a), ii) surface-step reconstruction induced by dislocation shearing (Figure 12b) or iii) a combination of both processes *i.e.,* part of the dislocation configuration under the indenter is blocked by a surface ledge while the rest multiplies and shears a nearby surface ledge. In this last case, the moving dislocation exerts a driving force on the rest of the emerging dislocation microstructure which unpins and concurrently gets absorbed by the closest lateral facet (Figure 12c). Note that the case where a dislocation nucleates and moves out of the sample without contact reaction with nearby surface steps (typical of

C_1=0.5) is also observed for C_1=1.2.

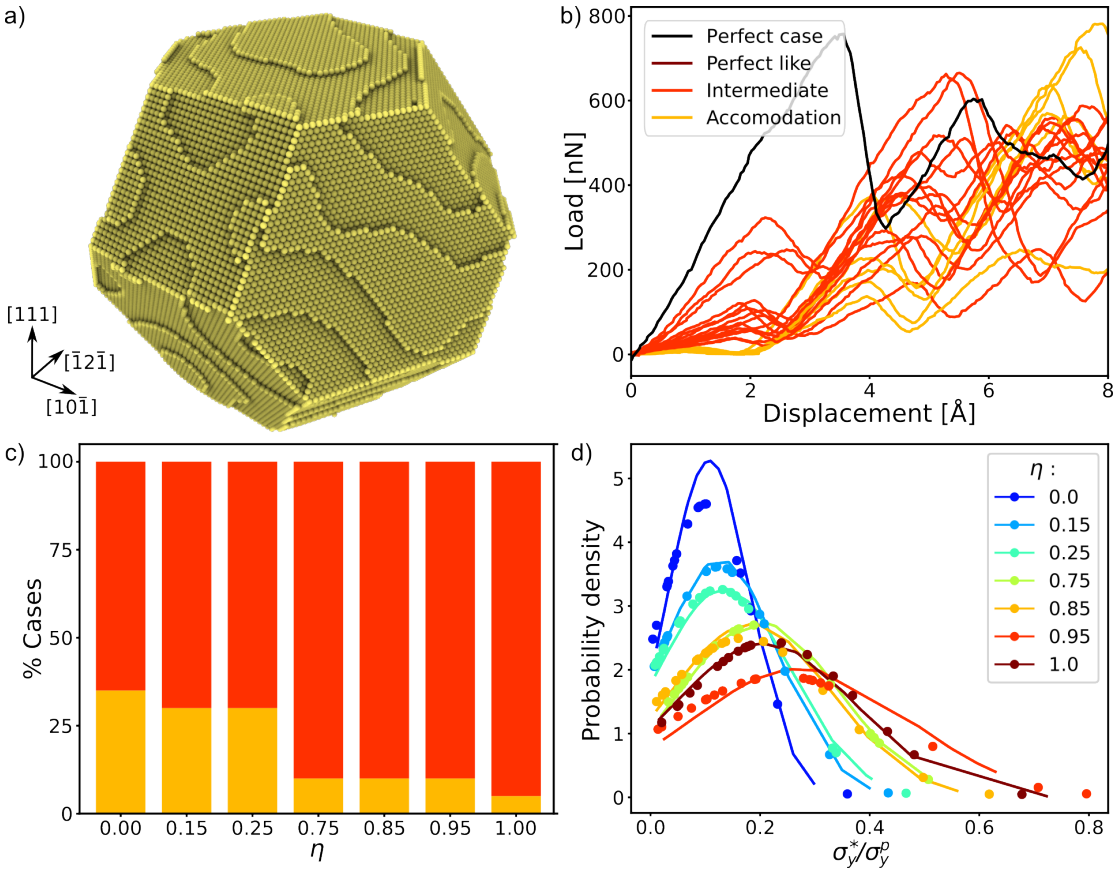

Figure 11: MD nanocompression of Au-faceted nanoparticles with wide surface roughness (C_1=1.2), a) example of nanoparticle (η=0.75), b) Load *vs.* displacement curves for η=0.25. The *perfect* case, *perfect-like*, *intermediate* and *accommodation* trends are illustrated in black, brown, red and yellow, respectively, c) Sample fraction distribution among *intermediate* and *accommodation* cases as a function of η (no *perfect-like* case), d) effective critical compressive stress σ_y^* distributions normalized by σ_y^p (*perfect* case) as a function of η. Symbols: MD simulations, curves: model (Equation 7).

5. Conclusion

Nanomechanics atomistic simulations are often based on simplistic designs made of flat facets and sharp edges or corners without considering the impact of these approximations on the sample strength and elementary deformation processes. In line with the recent studies that emphasized the role

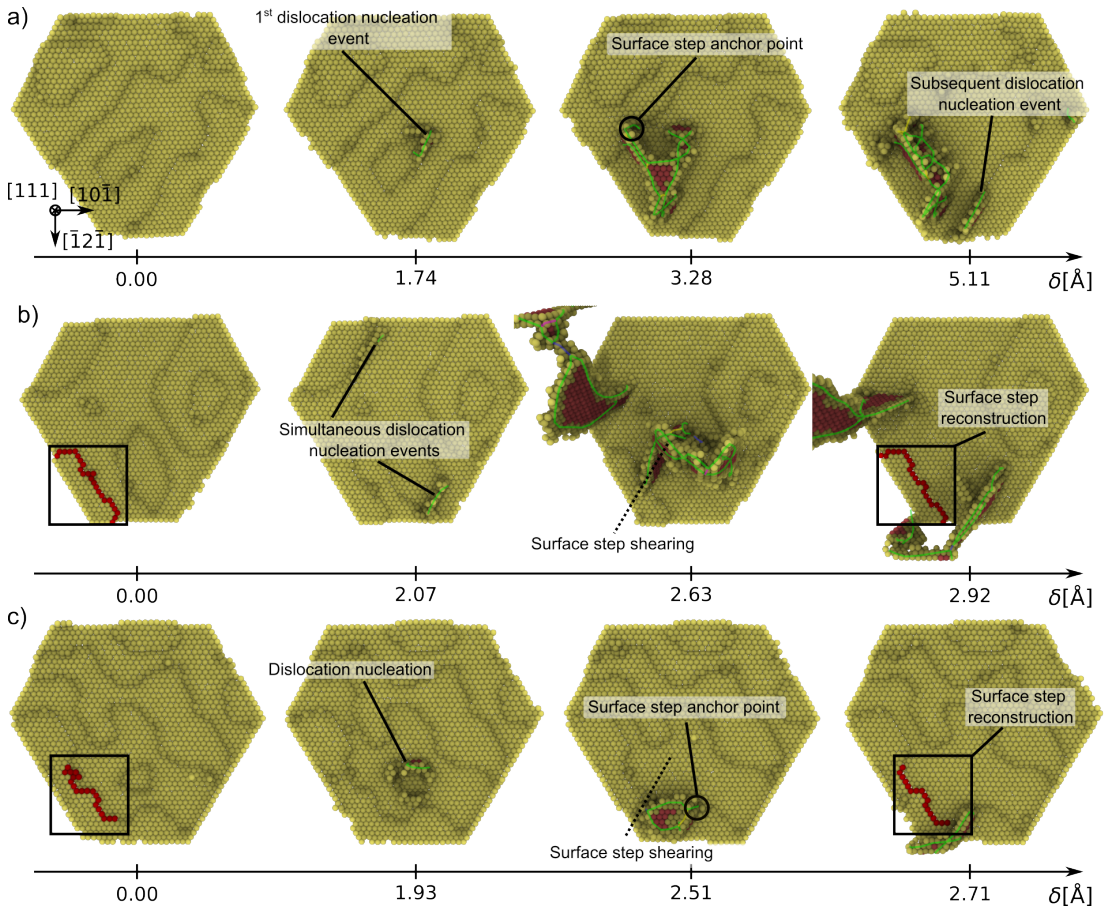

Figure 12: Examples of emerging dislocation microstructure evolution during MD nanocompression simulations of Au-faceted nanoparticles with wide surface roughness (C_1=1.2), a) surface step acting as an anchor point that locally impedes dislocation multiplication and promotes new nucleation events elsewhere on the surface, b) surface reconstruction induced by a dislocation shearing the surface ledge. One can note in this case the simultaneous nucleation of at least two dislocations, c) combination of both processes. View from below the top surface of the nanoparticle. Atoms colored in red denote zones of interest in case of surface ledge reconstruction induced by dislocation shearing.

of NPs shape on the mechanical properties [55, 65, 25], here we use a roughness model to design *in silico* NPs with rough surfaces that more rigorously describe the surface topology of metal or semi-conductor NPs used in the experiment. Here we show that even the lowest roughness (associated to a large roughness exponent) can dramatically impact the sample critical strength

that decreases by almost 90% for the roughest systems, when compared to the mean strength of flat-surface samples. This result provides some clues to explain the critical stresses data scattering regularly observed in nanoscale experiments, which can vary by one order of magnitude. Also, the numerous simulations performed allow to confirm that the yield force perfectly scales with the contact surface topography *i.e.,* the fraction of atoms in contact with indenter, bearing in mind a scaling factor transition for smaller contact regions where the shape of the first dislocation nucleated transits from a half- (isolated-islet regime) to a quarter-loop (edge-connected regime). Our statistical approach allows to design a model for strength dispersion predictions in case of sample with rough surfaces which only relies on two main inputs: 1) the characterisation of the top surface and 2) the ideal strength of the system, both of which can be deduced from experiment or theory. In addition, surface roughness has shown to be at the roots of exotic deformation processes in Au FCC metal NPs including dislocation nucleating and gliding in uncommon slip systems which may explain the recent observations made in experiments. In the future, more of these phenomena might be identified using *e.g.,* machine learning approaches, and new ideas based on surface topology characterization at the nanoscale are currently under investigation to better understand the mechanical properties of nano-objects in the experiments.

6. Acknowledgements

This work was supported by the Agence Nationale de la Recherche, grant no. ANR-20-CE09-0015 (ANR SASHA). The Fédération Lyonnaise de Modélisation et Sciences Numériques (FLMSN) and the Centre de Calcul Intensif d'Aix-Marseille are acknowledged for granting access to high performance computing resources. The authors would like to thank Pr. Mishin, Dr. Yastrebov and Dr. Pizzagalli for relevant discussions.

References

[1] J. Greer, C. Weinberger, W. Cai, Comparing the strength of fcc and bcc sub-micrometer pillars: compression experiments and dislocation dynamics simulations, Materials Science and Engineering A 493 (1) (2008) 21 – 25. doi:10.1016/j.msea.2007.08.093.

[2] S. H. Oh, M. Legros, D. Kiener, G. Dehm, In situ observation of dislocation nucleation and escape in a submicrometre aluminium single crystal, Nature Materials 8 (2) (2009) 95 – 100. doi:10.1038/nmat2370.

[3] O. Thomas, A. Ponchet, S. Forest, Mechanics of Nano-objects, Presses des MINES, 2011.

[4] A. T. Jennings, J. Li, J. R. Greer, Emergence of strain-rate sensitivity in Cu nanopillars: Transition from dislocation multiplication to dislocation nucleation, Acta Materialia 59 (14) (2011) 5627 – 5637. doi:10.1016/j.actamat.2011.05.038.

[5] S. Wang, Z. Shan, H. Huang, The Mechanical Properties of Nanowires, Advanced Science 4 (4) (2017) 1600332. doi:10.1002/advs.201600332.

[6] D. Mordehai, O. David, R. Kositski, Nucleation-controlled plasticity of metallic nanowires and nanoparticles, Advanced Materials 305 (2018) 1706710 – 17. doi:10.1002/adma.201706710.

[7] M. N. Esfahani, B. E. Alaca, A Review on Size-Dependent Mechanical Properties of Nanowires, Advanced Engineering Materials 21 (8) (2019) 1900192. doi:10.1002/adem.201900192.

[8] J. Amodeo, L. Pizzagalli, Modeling the mechanical properties of nanoparticles: a review, Comptes Rendus. Physique 22 (S3) (2021) 1–32. doi:10.5802/crphys.70.

[9] O. Kraft, P. A. Gruber, R. Mönig, D. Weygand, Plasticity in Confined Dimensions, Annual Review of Materials Research 40 (1) (2010) 293–317. doi:10.1146/annurev-matsci-082908-145409.

[10] J. R. Greer, J. T. De Hosson, Plasticity in small-sized metallic systems: Intrinsic versus extrinsic size effect, Progress in Materials Science 56 (6) (2011) 654–724. doi:10.1016/j.pmatsci.2011.01.005.

[11] D. Kiener, P. Hosemann, S. A. Maloy, A. M. Minor, In situ nanocompression testing of irradiated copper, Nature Materials 10 (8) (2011) 608–613. doi:10.1038/nmat3055.

[12] J. A. El-Awady, Unravelling the physics of size-dependent dislocation-mediated plasticity, Nature Communications 6 (1) (2015) 5926. doi:10.1038/ncomms6926.

[13] I. Issa, L. Joly-Pottuz, J. Amodeo, D. J. Dunstan, C. Esnouf, J. Réthoré, V. Garnier, J. Chevalier, K. Masenelli-Varlot, From dislocation nucleation to dislocation multiplication in ceramic nanoparticle, Materials Research Letters 9 (6) (2021) 278–283. doi:10.1080/21663831.2021.1894253.

[14] G. Richter, K. Hillerich, D. Gianola, R. Monig, O. Kraft, C. Volkert, Ultrahigh strength single crystalline nanowhiskers grown by physical vapor deposition, Nano Letters 9 (8) (2009) 3048 – 3052. doi:10.1021/nl9015107.

[15] T. Zhu, J. Li, A. Samanta, A. Leach, K. Gall, Temperature and Strain-Rate Dependence of Surface Dislocation Nucleation, Physical Review Letters 100 (2) (2008) 025502. doi:10.1103/PhysRevLett.100.025502.

[16] L. Y. Chen, M.-r. He, J. Shin, G. Richter, D. S. Gianola, Measuring surface dislocation nucleation in defect-scarce nanostructures, Nature Materials 14 (7) (2015) 707–713. doi:10.1038/nmat4288.

[17] Q.-J. Li, B. Xu, S. Hara, J. Li, E. Ma, Sample-size-dependent surface dislocation nucleation in nanoscale crystals, Acta Materialia 145 (2018) 19 – 29. doi:10.1016/j.actamat.2017.11.048.

[18] J. Amodeo, E. Maras, D. Rodney, Site dependence of surface dislocation nucleation in ceramic nanoparticles, npj Computational Materials 7 (1) (2021) 60. doi:10.1038/s41524-021-00530-8.

[19] M. D. Uchic, D. M. Dimiduk, J. N. Florando, W. D. Nix, Sample Dimensions Influence Strength and Crystal Plasticity, Science 305 (2004) 6. doi:10.1126/science.1098993.

[20] D. Mordehai, M. Kazakevich, D. J. Srolovitz, E. Rabkin, Nanoindentation size effect in single-crystal nanoparticles and thin films: A comparative experimental and simulation study, Acta Materialia 59 (6) (2011) 2309–2321. doi:10.1016/j.actamat.2010.12.027.

[21] D. Mordehai, S.-W. Lee, B. Backes, D. J. Srolovitz, W. D. Nix, E. Rabkin, Size effect in compression of single-crystal gold microparticles, Acta Materialia 59 (13) (2011) 5202–5215. doi:10.1016/j.actamat.2011.04.057.

[22] C. Carlton, L. Rabenberg, P. Ferreira, On the nucleation of partial dislocations in nanoparticles, Philosophical Magazine Letters 88 (9-10) (2008) 715–724. doi:10.1080/09500830802307641.

[23] I. Issa, J. Amodeo, J. Réthoré, L. Joly-Pottuz, C. Esnouf, J. Morthomas, M. Perez, J. Chevalier, K. Masenelli-Varlot, In situ investigation of MgO nanocube deformation at room temperature, Acta Materialia 86 (2015) 295–304. doi:10.1016/j.actamat.2014.12.001.

[24] S. Chen, F. Liu, B. Liu, X. Chen, X. Ke, M. Zhang, X. Tang, P. Guan, Z. Zhang, Z. Shan, Q. Yu, Reaching near-theoretical strength by achieving quasi-homogenous surface dislocation nucleation in MgO particles, Materials Today 55 (2022) 37–45. doi:10.1016/j.mattod.2022.04.007.

[25] A. Sharma, J. Hickman, N. Gazit, E. Rabkin, Y. Mishin, Nickel nanoparticles set a new record of strength, Nature Communications 9 (1) (2018) 4102. doi:10.1038/s41467-018-06575-6.

[26] S. Shahbeyk, G. Z. Voyiadjis, V. Habibi, S. H. Astaneh, M. Yaghoobi, Review of Size Effects during Micropillar Compression Test: Experiments and Atomistic Simulations, Crystals 9 (11) (2019) 591. doi:10.3390/cryst9110591.

[27] J. Zimmerman, A. Bisht, Y. Mishin, E. Rabkin, Size and shape effects on the strength of platinum nanoparticles, Journal of Materials Science 56 (32) (2021) 18300–18312. doi:10.1007/s10853-021-06435-7.

[28] K. Zheng, C. Wang, Y.-Q. Cheng, Y. Yue, X. Han, Z. Zhang, Z. Shan, S. X. Mao, M. Ye, Y. Yin, E. Ma, Electron-beam-assisted superplastic shaping of nanoscale amorphous silica, Nature Communications 1 (3) (2010) 1 – 8. doi:10.1038/ncomms1021.

[29] R. Soler, J. M. Molina-Aldareguia, J. Segurado, J. LLorca, R. I. Merino, V. M. Orera, Micropillar compression of LiF [111] single crystals: Effect of size, ion irradiation and misorientation, International Journal of Plasticity 36 (Supplement C) (2012) 50 – 63. doi:10.1016/j.ijplas.2012.03.005.

[30] M. Mačković, F. Niekiel, L. Wondraczek, E. Spiecker, Direct observation of electron-beam-induced densification and hardening of silica nanoballs

by in situ transmission electron microscopy and finite element method simulations, Acta Materialia 79 (2014) 363 – 373. doi:10.1016/j.actamat.2014.05.046.

[31] W. Gerberich, E. B. Tadmor, J. Kysar, J. A. Zimmerman, A. M. Minor, I. Szlufarska, J. Amodeo, B. Devincre, E. Hintsala, R. Ballarini, Review Article: Case studies in future trends of computational and experimental nanomechanics, Journal of Vacuum Science & Technology A: Vacuum, Surfaces, and Films 35 (6) (2017) 060801. doi:10.1116/1.5003378.

[32] S. Stangebye, Y. Zhang, S. Gupta, T. Zhu, O. Pierron, J. Kacher, Understanding and quantifying electron beam effects during in situ TEM nanomechanical tensile testing on metal thin films, Acta Materialia 222 (2022) 117441. doi:10.1016/j.actamat.2021.117441.

[33] C. Coupeau, J. Michel, J. Bonneville, M. Drouet, An atomic-scale insight into Ni_3Al slip traces, Materialia 9 (2020) 100563. doi:10.1016/j.mtla.2019.100563.

[34] V. S. Khoroshilov, D. M. Kazantsev, V. L. Alperovich, C. Coupeau, M. Drouet, Asymmetry of anticrossing between atomic steps on metal and semiconductor surfaces, Journal of Physics: Conference Series 2227 (1) (2022) 012008. doi:10.1088/1742-6596/2227/1/012008.

[35] S. Ijima, Electron Microscopy of Small Particles, Microscopy 34 (4) (1985) 249–265. doi:10.1093/oxfordjournals.jmicro.a050518.

[36] X. Y. Zhang, L. D. Zhang, Y. Lei, L. X. Zhao, Y. Q. Mao, Fabrication and characterization of highly ordered Au nanowire arrays, Journal of Materials Chemistry 11 (6) (2001) 1732–1734. doi:10.1039/b100552i.

[37] S.-H. Kim, H.-K. Kim, J.-H. Seo, D.-M. Whang, J.-P. Ahn, J.-C. Lee, Deformation twinning of ultrahigh strength aluminum nanowire, Acta Materialia 160 (2018) 14 – 21. doi:10.1016/j.actamat.2018.08.047.

[38] B. Mandelbrot, How Long Is the Coast of Britain? Statistical Self-Similarity and Fractional Dimension, Science 156 (3775) (1967) 636–638. doi:10.1126/science.156.3775.636.

[39] H. Iteney, J. A. Gonzalez Joa, C. Le Bourlot, T. W. Cornelius, O. Thomas, J. Amodeo, Pyrough: A tool to build 3D samples with rough

surfaces for atomistic and finite-element simulations, Computer Physics Communications (2024) 108958.doi:10.1016/j.cpc.2023.108958.

[40] Z.-J. Wang, Z.-W. Shan, J. Li, J. Sun, E. Ma, Pristine-to-pristine regime of plastic deformation in submicron-sized single crystal gold particles, Acta Materialia 60 (3) (2012) 1368 – 1377. doi:10.1016/j.actamat.2011.10.035.

[41] O. Kovalenko, C. Brandl, L. Klinger, E. Rabkin, Self-Healing and Shape Memory Effects in Gold Microparticles through the Defects-Mediated Diffusion, Advanced Science 4 (8) (2017) 1700159. doi:10.1002/advs.201700159.

[42] S. Roy, R. Gatti, B. Devincre, D. Mordehai, A multiscale study of the size-effect in nanoindentation of Au nanoparticles, Computational Materials Science 162 (2019) 47 – 59. doi:10.1016/j.commatsci.2019.02.013.

[43] F. Lauraux, S. Labat, M.-I. Richard, S. J. Leake, T. Zhou, O. Kovalenko, E. Rabkin, T. U. Schülli, O. Thomas, T. W. Cornelius, In Situ Nano-Indentation of a Gold Sub-Micrometric Particle Imaged by Multi-Wavelength Bragg Coherent X-ray Diffraction, Materials 15 (18) (2022) 6195. doi:10.3390/ma15186195.

[44] S. Plimpton, Fast Parallel Algorithms for Short-Range Molecular Dynamics, Journal of Computational Physics 117 (1) (1995) 1–19. doi:10.1006/jcph.1995.1039.

[45] A. P. Thompson, H. M. Aktulga, R. Berger, D. S. Bolintineanu, W. M. Brown, P. S. Crozier, P. J. i. t. Veld, A. Kohlmeyer, S. G. Moore, T. D. Nguyen, R. Shan, M. J. Stevens, J. Tranchida, C. Trott, S. J. Plimpton, LAMMPS - a flexible simulation tool for particle-based materials modeling at the atomic, meso, and continuum scales, Computer Physics Communications (2022) 108171doi:10.1016/j.cpc.2021.108171.

[46] G. Grochola, S. P. Russo, I. K. Snook, On fitting a gold embedded atom method potential using the force matching method, The Journal of Chemical Physics 123 (20) (2005) 204719. doi:10.1063/1.2124667.

[47] C. Deng, F. Sansoz, Near-Ideal Strength in Gold Nanowires Achieved through Microstructural Design, ACS Nano 3 (10) (2009) 3001 – 3008. doi:10.1021/nn900668p.

[48] H. Zheng, A. Cao, C. R. Weinberger, J. Y. Huang, K. Du, J. Wang, Y. Ma, Y. Xia, S. X. Mao, Discrete plasticity in sub-10-nm-sized gold crystals, Nature Communications 1 (9) (2010) 144 – 8. doi:10.1038/ncomms1149.

[49] M. Dupraz, G. Beutier, D. Rodney, D. Mordehai, M. Verdier, Signature of dislocations and stacking faults of face-centred cubic nanocrystals in coherent X-ray diffraction patterns: a numerical study, Journal of Applied Crystallography 48 (3) (2015) 621–644. doi:10.1107/s1600576715005324.

[50] S. Roy, S. Wille, D. Mordehai, C. A. Volkert, Investigating Nanoscale Contact Using AFM-Based Indentation and Molecular Dynamics Simulations, Metals 12 (3) (2022) 489. doi:10.3390/met12030489.

[51] H. Iteney, T. W. Cornelius, O. Thomas, J. Amodeo, Load versus displacement-controlled nanocompression: Insights from atomistic simulations, Scripta Materialia 226 (2023) 115245. doi:10.1016/j.scriptamat.2022.115245.

[52] J. Guénolé, W. G. Nöhring, A. Vaid, F. Houllé, Z. Xie, A. Prakash, E. Bitzek, Assessment and optimization of the fast inertial relaxation engine (fire) for energy minimization in atomistic simulations and its implementation in lammps, Computational Materials Science 175 (2020) 109584. doi:10.1016/j.commatsci.2020.109584.

[53] S. Azadehranjbar, R. Ding, I. M. P. Espinosa, A. Martini, T. D. B. Jacobs, Size-Dependent Role of Surfaces in the Deformation of Platinum Nanoparticles, ACS Nano 17 (9) (2023) 8133–8140. doi:10.1021/acsnano.2c11457.

[54] R. Ding, S. Azadehranjbar, I. M. P. Espinosa, A. Martini, T. D. B. Jacobs, Separating Geometric and Diffusive Contributions to the Surface Nucleation of Dislocations in Nanoparticles, ACS Nano 18 (5) (2024) 4170–4179. doi:10.1021/acsnano.3c09026.

[55] J. Amodeo, K. Lizoul, Mechanical properties and dislocation nucleation in nanocrystals with blunt edges, Materials & Design 135 (2017) 223–231. doi:10.1016/j.matdes.2017.09.009.

[56] A. Sharma, J. Amodeo, N. Gazit, Y. Qi, O. Thomas, E. Rabkin, When More Is Less: Plastic Weakening of Single Crystalline Ag Nanoparticles by the Polycrystalline Au Shell, ACS Nano 15 (2021-08-11) 14061. doi:10.1021/acsnano.1c02976.
URL https://pubs.acs.org/doi/10.1021/acsnano.1c02976

[57] A. M. Goryaeva, C. Fusco, M. Bugnet, J. Amodeo, Influence of an amorphous surface layer on the mechanical properties of metallic nanoparticles under compression, Physical Review Materials 3 (3) (2019) 033606. doi:10.1103/PhysRevMaterials.3.033606.

[58] Y. Mo, K. T. Turner, I. Szlufarska, Friction laws at the nanoscale, Nature 457 (7233) (2009) 1116–1119. doi:10.1038/nature07748.

[59] T. D. B. Jacobs, A. Martini, Measuring and Understanding Contact Area at the Nanoscale: A Review, Applied Mechanics Reviews 69 (6) (2017) 060802. doi:10.1115/1.4038130.

[60] C. Rycroft, Voro++: A three-dimensional Voronoi cell library in C++ (2009). doi:10.2172/946741.

[61] P. M. Larsen, S. Schmidt, J. Schiøtz, Robust Structural Identification via Polyhedral Template Matching, Modelling and Simulation in Materials Science and Engineering 24 (5) (2016) 055007. doi:10.1088/0965-0393/24/5/055007.

[62] A. Stukowski, Dislocation Analysis Tool for Atomistic Simulations, in: W. Andreoni, S. Yip (Eds.), Handbook of Materials Modeling, Springer International Publishing, 2018, pp. 1–14. doi:10.1007/978-3-319-42913-7_20-1.

[63] A. Stukowski, Visualization and analysis of atomistic simulation data with OVITO–the Open Visualization Tool, Modelling and Simulation in Materials Science and Engineering 18 (1) (2010) 015012. doi:10.1088/0965-0393/18/1/015012.

[64] W. H. Press, S. A. Teukolsky, Savitzky-Golay Smoothing Filters, Computers in Physics 4 (6) (1990) 669–672. doi:10.1063/1.4822961.

[65] D. Kilymis, C. Gérard, J. Amodeo, U. Waghmare, L. Pizzagalli, Uniaxial compression of silicon nanoparticles: An atomistic study on the shape and size effects, Acta Materialia 158 (2018) 155–166. doi:10.1016/j.actamat.2018.07.063.

[66] J. Amodeo, L. Pizzagalli, Modeling the mechanical properties of nanoparticles: A review, Comptes Rendus. Physique 22 (S3) (2021) 1–32. doi:10.5802/crphys.70.

[67] S. Brochard, P. Beauchamp, J. Grilhé, Dislocation nucleation from surface steps: Atomistic simulation in aluminium, Philosophical Magazine A 80 (3) (2000) 503–524. doi:10.1080/01418610008212065.

[68] P. Hirel, S. Brochard, L. Pizzagalli, P. Beauchamp, Effects of temperature and surface step on the incipient plasticity in strained aluminium studied by atomistic simulations, Scripta Materialia 57 (12) (2007) 1141–1144. doi:10.1016/j.scriptamat.2007.08.016.

[69] S. Hara, S. Izumi, S. Sakai, Reaction pathway analysis for dislocation nucleation from a Ni surface step, Journal of Applied Physics 106 (9) (2009) 093507. doi:10.1063/1.3254178.

[70] H. Lu, Y. Ni, J. Mei, J. Li, H. Wang, Anisotropic plastic deformation beneath surface step during nanoindentation of FCC Al by multiscale analysis, Computational Materials Science 58 (2012) 192–200. doi:10.1016/j.commatsci.2012.01.026.

[71] M.-I. Richard, S. Labat, M. Dupraz, J. Carnis, L. Gao, M. Texier, N. Li, L. Wu, J. P. Hofmann, M. Levi, S. J. Leake, S. Lazarev, M. Sprung, E. J. Hensen, E. Rabkin, O. Thomas, Anomalous Glide Plane in Platinum Nano- and Microcrystals, ACS Nano 17 (6) (2023) 6113–6120. doi:10.1021/acsnano.3c01306.

[72] K. W. Vugrin, L. P. Swiler, R. M. Roberts, N. J. Stucky-Mack, S. P. Sullivan, Confidence region estimation techniques for nonlinear regression in groundwater flow: Three case studies, Water Resources Research 43 (3) (2007) 2005WR004804. doi:10.1029/2005WR004804.

[73] Y. Feruz, D. Mordehai, Towards a universal size-dependent strength of face-centered cubic nanoparticles, Acta Materialia 103 (2016) 433–441. doi:10.1016/j.actamat.2015.10.027.